IAC–24–A6,9,3,x84335

A Pontryagin Neural Network Application to Tracklets Correlation of Optical Observations

Luca Ramponi[a]*, **Andrea D'Ambrosio**[b], **Riccardo Cipollone**[c], **Alessia De Riz**[d], **Roberto Furfaro**[e], **Vishnu Reddy**[f], **Pierluigi Di Lizia**[g]

[a] *Department of Aerospace Science and Technology, Politecnico di Milano, Via Giuseppe La Masa 34, Milan 20156, Italy, Department of Systems & Industrial Engineering, University of Arizona, 1127 E. James E. Rogers Way, Tucson, AZ 85721, USA, ramponiluca@outlook.it*
[b] *Department of Systems & Industrial Engineering, University of Arizona, 1127 E. James E. Rogers Way, Tucson, AZ 85721, USA, dambrosio@arizona.edu*
[c] *Department of Aerospace Science and Technology, Politecnico di Milano, Via Giuseppe La Masa 34, Milan 20156, Italy, riccardo.cipollone@polimi.it*
[d] *Department of Aerospace Science and Technology, Politecnico di Milano, Via Giuseppe La Masa 34, Milan 20156, Italy, alessia.deriz@polimi.it*
[e] *Department of Systems & Industrial Engineering, University of Arizona, 1127 E. James E. Rogers Way, Tucson, AZ 85721, USA, robertof@arizona.edu*
[f] *Department of Planetary Sciences - Lunar and Planetary Laboratory, University of Arizona, 1629 E. University Blvd., Tucson, AZ 85721, USA, vishnureddy@arizona.edu*
[g] *Department of Aerospace Science and Technology, Politecnico di Milano, Via Giuseppe La Masa 34, Milan 20156, Italy, pierluigi.dilizia@polimi.it*
* *Corresponding author*

Abstract

The increasing interest in the X-GEO region is leading towards a significant increment in its population of satellites and debris. Consequently, there will be a demand for techniques capable of accurately identifying, correlating, and cataloging X-GEO objects.

This paper introduces an innovative approach to solve tracklets correlation of optical observations via Pontryagin Neural Network (PoNN), which is a Physics-Informed Neural Network (PINN) trained to solve optimal control problems via indirect method and Pontryagin Minimum Principle. Within PoNN, the PINN framework called Extreme Theory of Functional Connections (X-TFC) is employed. PoNN is a particular kind of single-layer feed-forward neural network used to estimate the object's state and costate, while solving an energy optimal control problem. Indeed, since no maneuvering objects are considered, the ballistic trajectory, solution of the successfully correlated tracklets, is assumed to be the one minimizing the control effort. The correlation is assessed through a criterion based on the Mahalanobis distance, involving the residuals on the observations and the DeltaV associated to the computed optimal trajectory.

The proposed method is applied to angles-only observations of objects in Keplerian dynamics and tested on both simulated and real data. For the case of real data, the majority of the real topocentric right ascension and declination measurements have been provided by the telescopes of the Space4 Center at the University of Arizona.

Keywords: Space Situational Awareness, Optical Tracklets Correlation, Pontryagin Neural Networks, Physics-Informed Neural Networks, Uncertainty Propagation

1. Introduction

The rapid increase in satellite numbers, the growth of the commercial space industry, and the persistent problem of space debris present significant challenges that demand innovative solutions. Central to these solutions is the concept of Space Situational Awareness (SSA), a comprehensive framework dedicated to monitoring, analyzing, and predicting the behavior of objects and events in space ([1]). Although current SSA efforts are largely concentrated on the near-Earth environment, the growing interest in missions targeting the X-GEO region, such as Artemis, underscores the future need for techniques capable of accurately identifying, correlating, and cataloging objects in these remote areas of space. Unfortunately, traditional methods based on two-body dynamical features, which work well in near-Earth scenarios, are not easily adaptable to the more complex dynamical environments of the X-GEO region. Therefore, the development of new techniques based on universal principles, applicable across various dynamical models, will be essential. The processes of detecting, identifying, and determining the orbits of celestial objects are crucial for successful SSA operations. Within

this context, optical surveys are particularly valuable tools. Indeed, radar systems are not feasible for remote regions such as X-GEO due to their limited power capabilities, rendering them unsuitable for such applications. Because of these challenges, optical telescopes or space-based observation platforms are typically used to monitor objects in the X-GEO region. During such surveys, telescopes scan the sky to detect objects moving against a background of stationary stars. As these objects move, they create streaks, or tracklets, which are recorded against the field of fixed stars (Fig. 1). However, according to the system, some telescopes are able to target a specific object and follow its motion. Thus, in this scenario, the observed object would be represented by a dot in a background of streaks (i.e. stars).

Fig. 1. Image from optical survey ([2]). The streaks represent tracklets against a fixed star background.

Once a tracklet is detected, its topocentric right ascension (α) and declination (δ) are determined through astrometric reduction, using the catalogued positions of stars as a reference. Typically, surveys produce numerous observations of various celestial objects, often resulting in only a small amount of data for each one. Additionally, the precision of these measurements can be affected by factors such as instrumentation error, atmospheric conditions, and inaccuracies in astrometric reduction. This underscores the importance of accurately identifying and correlating independent observations that belong to the same physical object. The following paper addresses the linkage problem of optical observations, which involves arcs of measurements, called Too Short Arcs (TSAs), that are too short to achieve angles-only orbit determination with high accuracy using classical methods like those of Laplace ([3]), Gauss ([4]), and their derivatives ([5]). Thus, the preliminary step of correlation is crucial to verify the association between two tracklets.

Several methods have been developed to tackle the tracklet association problem. These methods generally involve assuming some of the unknown free parameters to obtain an initial orbit estimate. The candidate orbits are then tested and either accepted or rejected based on their accuracy.

One approach to solve the linkage problem is the Virtual Debris Algorithm, introduced by Tommei et al. [6], which is based on the Admissible Region (AR) theory first proposed by Milani to specifically address short arcs of observations ([7]). Within this context, a tracklet is usually represented by means of an attributable, which condenses the series of angles-only observations into a single couple of angles and angular velocities at a given time. Thus, the only missing variables are the range ρ and range-rate $\dot{\rho}$. The AR is a tool to define constraints on the possible values of the unknowns in a linkage problem. By assuming that the optical observations belong to a satellite orbiting the Earth, physical constraints can be imposed to limit the solution space of the pair $(\rho, \dot{\rho})$ at a specific epoch ([7]-[8]). Despite these constraints, the AR still defines an infinite set of possible solutions, necessitating an efficient sampling technique to generate a series of Virtual Space Objects (VSOs). From these, candidate solutions are generated by propagating each VSO to the epoch of the second arc along with the associated covariance matrix. Candidate solutions are then either discarded or retained based on an attribution penalty ([9]-[10]).

As an alternative to this first approach, Gronchi et al. introduced a method based on the first integrals of Kepler's problem—the angular momentum and energy integrals ([11]). They later refined this approach ([12]) by replacing the energy integral with a component of the Laplace-Lenz vector, thereby improving computational efficiency. Both methods rely on the principle that, under Keplerian dynamics, the integrals of motion are conserved. These algorithms address the linkage problem between sets of astrometric observations expressed through attributables. Given two attributables assumed to belong to the same object, polynomial expressions for the ranges and range-rates at two epochs are derived using Keplerian integrals. The process involves equating the integrals of motion at the two epochs, leading to a system of nonlinear equations in the variables (ρ_0, ρ_f), which is solved using a Discrete Fourier Transform (DFT) and its inverse. Compatibility conditions are then applied to verify whether the initial hypothesis that the tracklets belong to the same object holds, discarding solutions associated with different bodies. The IOD technique described in [13] further reduces computational complexity by utilizing Differential Algebra (DA).
Additionally, a recent study ([14]) introduces a DA-based approach that leverages Automatic Domain Split-

ting (ADS) and the AR to handle optical attributables by searching for the minimum energy trajectory linking them.

However, existing techniques are heavily dependent on the two-body dynamics, either through the use of the admissible region or by relying on the conservation of Keplerian parameters. This paper presents an innovative method to tackle the tracklet correlation problem, firstly introduced in ([14]), less reliant on the specific problem's dynamics, thus enabling future extensions of the algorithm to X-GEO applications. The proposed framework is applied to both simulated data, for validation purposes, and to real observations, mostly provided by the Space4 Center at The University of Arizona. A similar formulation of the control distance metric introduced by Holzinger et al. ([15]) is employed for non-maneuvering geostationary (GEO) satellites, where the solution is assumed to be the one computed by solving the energy optimal problem between two tracklets. Thus, the linkage problem of optical observations is solved via Pontryagin Neural Network (PoNN, [16]), a type of Physics-Informed Neural Network (PINN) designed to solve optimal control problems via indirect method and Pontryagin Minimum Principle (PMP). PINN is a framework developed by Raissi et al. ([17]) for approximating solutions to general nonlinear PDEs, while exploiting the prior information coming from the physical laws governing the system's dynamics as a regularization term that constrains the space of admissible solutions. This methodology leverages the well-established capability of neural networks (NNs) as universal function approximators, allowing for the effective handling of nonlinear problems without relying on predetermined assumptions ([18]-[19]). Within PoNN, the PINN framework called Extreme Theory of Functional Connections (X-TFC, [20]) is employed. Although it is an already proven method for orbit determination regardless of the problem's dynamics, exhibiting fast and robust convergence to highly accurate results ([21]- [22]), its application to tracklets correlation problems has not yet been investigated. Here, a PoNN-based approach has proven effective for solving track-to-track association problems for objects following two-body dynamics. However, the dynamics does not represent a limitation as the developed framework can be easily extended to other dynamical regimes, as shown by the cited references. The foundational theory supporting the methodology is outlined in Section 2 and 3, along with a detailed explanation of the developed procedure. Section 4 presents the results obtained by applying the method to both simulated and real data of non-maneuvering GEO satellites. Section 5 concludes the research by drawing final considerations and discussing potential directions for future developments.

2. Energy Optimal Control Problem

An optimal control problem is usually based on a cost function expressed as ([23]):

$$\mathcal{J} = \mathbf{\Phi}(x_0, t_0, x_f, t_f) + \int_{t_0}^{t_f} \mathcal{L}(\boldsymbol{x}(t), \boldsymbol{u}(t), t)dt \quad (1)$$

where $\mathbf{\Phi}$ is the terminal cost, while $\mathcal{L}$ is the Lagrangian defining the integral cost over the trajectory. These are function of the state vector $\boldsymbol{x}(t)$, the control vector $\boldsymbol{u}(t)$ and the independent variable t. Assuming to have an energy optimal problem, it can be rewritten such that it aims at finding the control acceleration $\boldsymbol{u}(t)$ that minimizes:

$$\mathcal{J} = \frac{1}{2} \int_{t_0}^{t_f} \boldsymbol{u}(t)^T \boldsymbol{u}(t)dt \quad (2)$$

subjected to the problem's dynamics and boundary conditions at the initial and final time epochs, denoted as t_0 and t_f respectively:

$$\begin{cases} \dot{\boldsymbol{x}} = f(t, \boldsymbol{x}(t), \boldsymbol{u}(t)) \\ \mathbf{\Phi}(x(t_0), t_0) = \mathbf{\Phi}_0 \\ \mathbf{\Phi}(x(t_f), t_f) = \mathbf{\Phi}_f \end{cases} \quad (3)$$

The Hamiltonian scalar function can be defined as:

$$\mathcal{H} = \frac{1}{2}\boldsymbol{u}(t)^T \boldsymbol{u}(t) + \boldsymbol{\lambda}^T \boldsymbol{f}(t, \boldsymbol{x}(t), \boldsymbol{u}(t)) \quad (4)$$

where $\boldsymbol{\lambda}$ is the costate vector. Therefore, the first-order necessary conditions for optimality, together with the optimal control obtained through the PMP, are written as follows:

$$\begin{cases} \dot{\boldsymbol{x}} = \mathcal{H}_{\boldsymbol{\lambda}} \\ \dot{\boldsymbol{\lambda}} = -\mathcal{H}_{\boldsymbol{x}} \\ 0 = \mathcal{H}_{\boldsymbol{u}} \end{cases} \quad (5)$$

The set of differential equations above, whose first two are known as the Euler-Lagrange (E-L) equations, along with the boundary conditions, constitute the comprehensive problem formulation. According to the analyzed problem, some transversality conditions on the Hamiltonian and/or on the adjoint variables might also have to be satisfied. They complement the necessary conditions for optimality by providing further necessary boundary conditions according to whether the initial/final states and times are free or fixed:

- Free state:

$$\boldsymbol{\lambda}_f = \frac{\partial \mathbf{\Phi}(\boldsymbol{x}_f, t_f)}{\partial \boldsymbol{x}_f} \quad (6)$$

- Free time:

$$H(\boldsymbol{x}_f, \boldsymbol{u}_f, \boldsymbol{\lambda}_f, t_f) + \frac{\partial \boldsymbol{\Phi}(\boldsymbol{x}_f, t_f)}{\partial t_f} = 0 \quad (7)$$

Upon successfully recovering the optimal control $\boldsymbol{u}^*$ as an explicit function of state and costate by solving the third equation in 5, the original energy optimal problem (EOP) is effectively rewritten into a two-point boundary value problem (TPBVP) in terms of just the state $\boldsymbol{x}$ and costate $\boldsymbol{\lambda}$.

3. Pontryagin Neural Network

Pontryagin Neural Networks (PoNNs) are PINN specifically designed to solve optimal control problems via indirect methods and PMP ([16]). Once the problem is trasformed into a two-point boundary value problem by deriving the first-order necessary optimality conditions and the optimal control through the PMP, the optimal control actions are learnt from the unknown solutions of the TPBVP, modeled within the PoNN framework. Specifically, the PINN approach adopted is X-TFC. The Extreme Theory of Functional Connections, introduced by Schiassi et al. ([20]), combines the advantages of PINNs and the Theory of Functional Connections (TFC). An overview of the PoNN framework is summarized in Fig. 2 and explained below.

PoNN exploits a functional interpolation method, called TFC, developed by Mortari in [24]. It consists in deriving an analytical expression, known as functional, that represents all functions satisfying a given set of constraints. The resulting expression, referred to as a Constrained Expression (CE), is formulated as the sum of a free function and a functional that respects the imposed constraints ([25]):

$$y(t, g(t)) = g(t) + \sum_{k=1}^{n_k} \phi_k(t) \rho_k(t, g(t)) \quad (8)$$

where n_k is the number of constraints applied on the unknown variable y and $g(t)$ is the free function. The second term of the right-hand side is composed by the switching functions $\phi_k(t)$ and the projection functionals $\rho_k(t, g(t))$. A projection functional quantifies the difference between the constraint value and the evaluation of the free function at that constraint. The switching functions are designed to be 1 at their respective constraints and 0 at any others. Traditionally, the TFC approach uses a free function that is a linear combination of orthogonal polynomials, such as Chebyshev polynomials, due to their approximation and convergence benefits. However, these methods can become problematic with increasing problem dimensionality. In the X-TFC framework, the objective

remains to approximate the DE solution through a TFC constrained expression, but with a neural network chosen as the free function. This approach addresses the curse of dimensionality, enabling precise solutions for large-scale problems with reduced computational time, while categorizing X-TFC as a PINN framework. Specifically, as illustrated in step 4 of Fig. 2, the method employs a Single Layer Feed-Forward Neural Network (SLFN) trained via the Extreme Learning Machine (ELM) algorithm. The Extreme Learning Machine (ELM), proposed by Huang et al. ([26]), is a training algorithm for SLFN where input weights (w_i) and biases (b_i) are randomly initialized and kept constant, while only the output weights (β_i) are trained. These are computed using a Least-Squares (LS) method, which significantly reduces the computational time ([23]). ELMs combine the approximation power of deep neural networks with faster training and enhanced generalization performance. Indeed, ELMs are also supported by the universal approximation theorem ([27]).

Therefore, in a X-TFC framework the free function is expressed as:

$$g(z) = \sum_{i=1}^{L} \beta_i \sigma(w_i^T z + b_i) \quad (9)$$

where z is the domain of the nonlinear activation functions σ in which the independent variable t is mapped, and L defines the number of neurons of the hidden layer. Since the neural network training is performed with the ELM algorithm, the only unknowns to compute are the output weights $\boldsymbol{\beta}$, while w_i and b_i are randomly assigned. Assuming to have n collocation times $\boldsymbol{t}_l (l = 1, .., n)$ of the training set, it is possible to introduce the matrix $\boldsymbol{H}$, also called hidden layer matrix, which $i - th$ column is associated to the $i - th$ neuron and the $l - th$ row for the $l - th$ input. Thus, the output is:

$$\boldsymbol{G} = \boldsymbol{H}(\boldsymbol{z})\boldsymbol{\beta} = [\boldsymbol{h}(z_1), \boldsymbol{h}(z_2), ..., \boldsymbol{h}(z_n)]^T \boldsymbol{\beta} \quad (10)$$

where

$$\boldsymbol{h}(z_l) = [\sigma(w_1^T z_l + b_1), \sigma(w_2^T z_l + b_2), ..., \sigma(w_L^T z_l + b_L)]$$

Consequently, in compliance with the TFC, the differential equation's (DE) latent solution is approximated through a constrained expression analytically satisfying the constraints, as described by Eq. 8. By substituting the CE into the constrained system's differential equations, the problem becomes unconstrained and it is reformulated in terms of the free function $g(t)$ and its derivatives.

Moreover, as a physics-informed method, X-TFC includes a loss function for the problem's dynamics (step 6). Here, the physics governing the data acts as a regular-
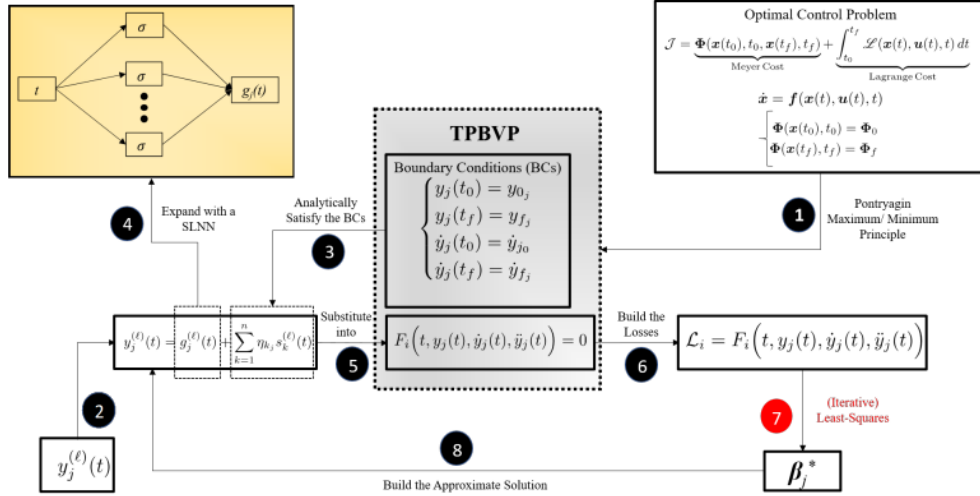
Fig. 2. PoNN framework ([23]). Once the TPBVP is formulated, the X-TFC is applied through steps (3,4,5) by defining the CEs, using as free function $g(t)$ a NN trained via ELM. The output weights $\boldsymbol{\beta}$ are optimized via nonlinear solvers, minimizing the loss vector.

ization term during the training by preventing the neural network from violating the physics.

Finally, the output layer weights $\boldsymbol{\beta}$ are learnt via LS or, in case of nonlinear problems, an iterative LS procedure is applied. Hereafter, the MatLab function *lsqnonlin*, which includes advanced algorithms such as the Levenberg-Marquardt method, is employed to accurately compute the optimal output weights of PoNN, especially for problems involving significant non-linearities.

The application of the X-TFC algorithm to learn the solution of the TPBVP, obtained by applying the indirect method and PMP to an OCP, represents the PoNN method. It is important to emphasize that the procedure does not require any prior orbit information since the convergence is ensured for randomly initialized weights and biases. This feature enables the method to function effectively even when there is minimal prior knowledge about the object's orbit.

3.1 Application to correlation problem

The available data consist of collections of three optical observations composed of pairs of topocentric right ascension and declination $(\boldsymbol{\alpha}, \boldsymbol{\delta})$, which are referred to as tracklets. In this context, PoNN is employed to determine the solution of an energy optimal trajectory using two tracklets as boundary conditions, hereafter named nominal trajectory. For clarity, the methodology is divided into three distinct phases: solution of the EOP via PoNN, uncertainty analysis and correlation assessment, as shown in Fig. 3.
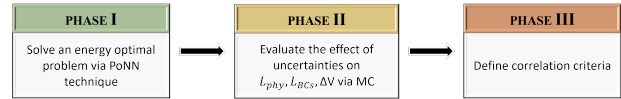

Fig. 3. Flowchart PoNN correlation method ([14]). Phase 1: solution of the energy optimal problem. Phase 2: uncertainty analysis. Phase 3: correlation assessment.

The quantities involved are dimensionless to improve convergence to the solution. After setting the time constant TU as the time interval between the first and last observations (ToF), the distance constant LU is selected so that the dimensionless gravitational parameter μ_{adim} equals 1, as reported in Table 1.

TU (s)	LU (Km)	μ_{adim}
ToF	$\sqrt[3]{(\mu\ TU^2)}$	1.0

Table 1. Adimensionalizing constants (PoNN).

3.1.1 Phase I: Energy optimal trajectory

Initially, the energy optimal trajectory connecting two tracklets, called nominal trajectory, is computed. Recalling that each tracklet is composed of three optical observations $(\boldsymbol{\alpha}, \boldsymbol{\delta})$, these represent the boundary conditions of the problem.

Fig. 4 shows the steps followed to solve the optimization problem.

Fig. 4. Flowchart Phase I ([14]). Overview of the procedure to solve the EOP with PONN.

Given that the dataset consists of observations of GEO satellites, the analysis assumes the following unperturbed two-body dynamics: $\boldsymbol{f}(t, \boldsymbol{x}(t), \boldsymbol{u}(t))$, where $\boldsymbol{u}$ represents the control acceleration vector, and $\boldsymbol{r}$ and $\boldsymbol{v}$ are the position and velocity vectors, respectively:

$$\begin{cases} \dot{\boldsymbol{r}} = \boldsymbol{v} \\ \dot{\boldsymbol{v}} = -\frac{\mu}{r^3}\boldsymbol{r} + \boldsymbol{u} \end{cases} \tag{11}$$

Recalling Eq. 5, the Euler-Lagrange equations and the optimal control are written as:

$$\begin{cases} \dot{\boldsymbol{x}} = \boldsymbol{f}(t, \boldsymbol{x}(t), \boldsymbol{u}(t)) \\ \dot{\boldsymbol{\lambda}} = -\boldsymbol{A}\boldsymbol{\lambda} \\ 0 = \mathcal{H}_{\boldsymbol{u}} \end{cases} \tag{12}$$

where $\boldsymbol{x} = [\boldsymbol{r}, \boldsymbol{v}]^T$ and $\boldsymbol{\lambda} = [\boldsymbol{\lambda}_r, \boldsymbol{\lambda}_v]^T$ are the state and costate vectors, respectively. The matrix $\boldsymbol{A}$ is defined as the partial derivative of the dynamics with respect to the state:

$$\boldsymbol{A} = \left[\frac{\partial \boldsymbol{f}(t, \boldsymbol{x}(t), \boldsymbol{u}(t))}{\partial \boldsymbol{x}} \right]^T \tag{13}$$

$$= \begin{bmatrix} \boldsymbol{0}_{3\times3} & \frac{3\mu}{r^5}\boldsymbol{r}^T\boldsymbol{r} - \frac{\mu}{r^3}\boldsymbol{I}_{3\times3} \\ \boldsymbol{I}_{3\times3} & \boldsymbol{0}_{3\times3} \end{bmatrix} = \begin{bmatrix} \boldsymbol{0}_{3\times3} & \boldsymbol{B} \\ \boldsymbol{I}_{3\times3} & \boldsymbol{0}_{3\times3} \end{bmatrix}$$

Thus, the TPBVP is ultimately formulated as:

$$\begin{cases} \dot{\boldsymbol{x}} = \boldsymbol{f}(t, \boldsymbol{x}(t), \boldsymbol{u}(t)) \\ \dot{\boldsymbol{\lambda}}_r = -\boldsymbol{B}\boldsymbol{\lambda}_v \\ \dot{\boldsymbol{\lambda}}_v = -\boldsymbol{\lambda}_r \\ \boldsymbol{u} = -\boldsymbol{\lambda}_v \end{cases} \tag{14}$$

However, certain inter-dependencies among the variables can be observed. This enables further simplifications of the problem by reducing the number of independent variables that need to be considered. Consequently, the equations of motion are condensed to focus on the subset defining the position $\boldsymbol{r}$ and the costate associated with the velocity $\boldsymbol{\lambda}_v$:

$$\begin{cases} \ddot{\boldsymbol{r}} = -\frac{\mu}{r^3}\boldsymbol{r} - \boldsymbol{\lambda}_v \\ \ddot{\boldsymbol{\lambda}}_v = \boldsymbol{B}\boldsymbol{\lambda}_v \end{cases} \tag{15}$$

The TPBVP is considered complete once the transversality conditions are specified. Given that both the initial and final times are fixed by the measurement epochs, conditions in the form of Eq. 7 are not applicable. However, since the initial and final states are unknown, the transversality conditions for the position vector are derived and translated into constraints on $\boldsymbol{\lambda}_v$:

$$\begin{cases} \boldsymbol{\lambda}_r(t_0) = \boldsymbol{0} \rightarrow \dot{\boldsymbol{\lambda}}_v(t_0) = \boldsymbol{0} \\ \boldsymbol{\lambda}_r(t_f) = \boldsymbol{0} \rightarrow \dot{\boldsymbol{\lambda}}_v(t_f) = \boldsymbol{0} \end{cases} \tag{16}$$

As detailed in Section 3, the X-TFC framework is used to approximate the latent solutions of the problem. According to Eq. 15, due to the dependencies among the variables, only $\boldsymbol{\lambda}_v$ and $\boldsymbol{r}$ need to be approximated using constrained expressions, while the remaining variables can be recovered afterward. Once the outer weights of the neural network, $\boldsymbol{\beta}$, are determined, all the quantities can be retrieved.

In order to define the constrained expressions, a linear mapping from the time domain t to the domain z of the activation functions in the interval $[-1, 1]$ is introduced:

$$z = z_0 + c(t - t_0) \tag{17}$$

where $c = (z_f - z_0)/(t_f - t_0)$ is a constant allowing to switch from one domain to the other.

Since no constraints are applied, the constrained expressions for the position $\boldsymbol{r}$ consists solely of the free function:

$$\boldsymbol{x}(t) = \boldsymbol{H}(z)\boldsymbol{\beta}_x \qquad \boldsymbol{y}(t) = \boldsymbol{H}(z)\boldsymbol{\beta}_y$$
$$\boldsymbol{z}(t) = \boldsymbol{H}(z)\boldsymbol{\beta}_z \tag{18}$$

having defined the free function $g(t)$ and its derivatives as:

$$\boldsymbol{g}(t) = \boldsymbol{H}(z)\boldsymbol{\beta}_{(\cdot)} \qquad \dot{\boldsymbol{g}}(t) = c\boldsymbol{H}'(z)\boldsymbol{\beta}_{(\cdot)}$$
$$\ddot{\boldsymbol{g}}(t) = c^2\boldsymbol{H}''(z)\boldsymbol{\beta}_{(\cdot)} \tag{19}$$

The hidden layer matrix $\boldsymbol{H}(z)$ has dimensions $n \times L$, where n denotes the number of collocation points along the time vector and L represents the number of neurons in the hidden layer. For a generic variable k, the outer weights vector $\boldsymbol{\beta}_k$ has a length equal to the chosen number of neurons. Thus, the variable is computed by multiplying the matrix $\boldsymbol{H}(z)$ by the corresponding output weights. In contrast, the transversality conditions (Eq. 16) are im-

posed on the variables $\boldsymbol{\lambda}_{v_i}$ $(i = x, y, z)$. Thus, the associated constrained expressions are expressed as:

$$\boldsymbol{\lambda}_{v_i}(t, \boldsymbol{g}(t)) = \boldsymbol{g}(t) + \phi_3(t)\rho_3(t_0, g_0) + \phi_4(t)\rho_4(t_f, g_f) \tag{20}$$

Therefore:

$$\boldsymbol{\lambda}_{v_i}(t) = \boldsymbol{\Phi}(z)\boldsymbol{\beta}_{v_i} \tag{21}$$

$$\boldsymbol{\Phi}_{n \times L}(z) = \left[\boldsymbol{H} - \phi_3 \boldsymbol{H'_0} - \phi_4 \boldsymbol{H'_f} \right]^T \tag{22}$$

where the derivatives of $\boldsymbol{H}$ are performed in the z domain. The terms $\boldsymbol{H'_0}$, $\boldsymbol{H'_f}$ refer to the first and last rows of the derivative of the matrix $\boldsymbol{H}$, respectively.

Recalling that X-TFC is a physics-informed method, the loss vector is included in the formulation. It takes into account the observations residuals as well as a regularization term which ensures that the orbital dynamics is respected. Therefore, the relation input/output is encouraged to be compliant with the physics, while fitting the observations. The following three contributions are considered:

- Physics ($\boldsymbol{L}_{phy}$): the physics component serves as a regularization term, facilitating convergence and ensuring that the results comply with the laws of dynamics.

$$\boldsymbol{L}_{\ddot{r}} = \ddot{\boldsymbol{r}} + \frac{\mu}{r^3}\boldsymbol{r} + \boldsymbol{\lambda}_v \tag{23}$$

$$\boldsymbol{L}_{\ddot{\lambda}_v} = \ddot{\boldsymbol{\lambda}}_v - \boldsymbol{B}\boldsymbol{\lambda}_v \tag{24}$$

- BCs ($\boldsymbol{L}_{BCs}$): since incorporating boundary conditions that are nonlinear functions of the states approximated through the CE directly into the constrained expressions presents significant challenges, these loss terms are added to ensure that the solution matches the available optical observations. Thus, for each couple $(\bar{\alpha}, \bar{\delta})$:

$$\boldsymbol{L}_{\sin\alpha} = \sin\bar{\alpha} - \sin\alpha_{NN} \tag{25}$$
$$\boldsymbol{L}_{\cos\alpha} = \cos\bar{\alpha} - \cos\alpha_{NN} \tag{26}$$
$$\boldsymbol{L}_{\sin\delta} = \sin\bar{\delta} - \sin\delta_{NN} \tag{27}$$

where the subscript *NN* defines the angles estimated with the neural network. Here, trigonometric functions of the angles are used to prevent ambiguities.

- Energy: enforcing the minimization of energy to find the best optimal solution:

$$L_E = \frac{1}{2}\int_{t_0}^{t_f} \boldsymbol{u}(t)^T \boldsymbol{u}(t)dt \tag{28}$$

Thus, by applying the weights $(\boldsymbol{W}_{phy}, \boldsymbol{W}_{BCs}, W_E)$ to scale the influence of each contribution differently, the loss vector is given by:

$$\mathbb{L} = [\boldsymbol{W}_{phy}\boldsymbol{L}_{phy}, \boldsymbol{W}_{BCs}\boldsymbol{L}_{BCs}, W_E L_E] \tag{29}$$

The nominal solution is retrieved by computing the optimal parameters $\bar{\boldsymbol{\beta}}$ minimizing the loss vector, where:

$$\bar{\boldsymbol{\beta}} = \left[\bar{\boldsymbol{\beta}}_x, \bar{\boldsymbol{\beta}}_y, \bar{\boldsymbol{\beta}}_z, \bar{\boldsymbol{\beta}}_{v_x}, \bar{\boldsymbol{\beta}}_{v_y}, \bar{\boldsymbol{\beta}}_{v_z} \right]^T \tag{30}$$

The energy optimization problem is tackled by finding $\bar{\boldsymbol{\beta}}$ using a nonlinear least squares method, specifically the Levenberg-Marquardt algorithm, through the MatLab function *lsqnonlin*. In this study, the $\boldsymbol{\beta}_0$ values are randomly initialized within the range of -1 to 1.

The cost ΔV_{nom} associated with the nominal trajectory is then calculated based on the energy and the time distance separating the tracklets, as outlined in [15] ([28]):

$$\Delta V_{nom} = \sqrt{2E \times (ToF)} \tag{31}$$

3.1.2 Phase II: Uncertainty analysis

Phase II focuses on evaluating the impact of the uncertainties affecting the optical observations. The main objective is to understand how these uncertainties influence the quantities of interest that are used to define the correlation index.

This study aims to evaluate the correlation of 2 tracklets by means of a metric based on the distance between quantities related to the nominal trajectory and distributions of the same quantities stemming from tracklet uncertainty only. For this reason, this assessment is performed along the ballistic trajectory (i.e. zero energy) simulated from the optimal initial state $\boldsymbol{x}_0$ determined in Phase I. This procedure is used to exclude the influence of additional errors present in real observations.

According to the scheme outlined in Fig. 5, after obtaining the simulated measurements at the same epochs as the real data, a Monte Carlo simulation is carried out using the MatLab function *mvnrnd*. Therefore, multiple samples $n_{samples}$ of the simulated observations $(\boldsymbol{\alpha}, \boldsymbol{\delta})$ are generated assuming a gaussian distribution described by the instrumentation's accuracy $(\sigma_\alpha, \sigma_\delta)$:

$$\sigma_\alpha = \sigma_\delta = 10^{-6} rad \tag{32}$$
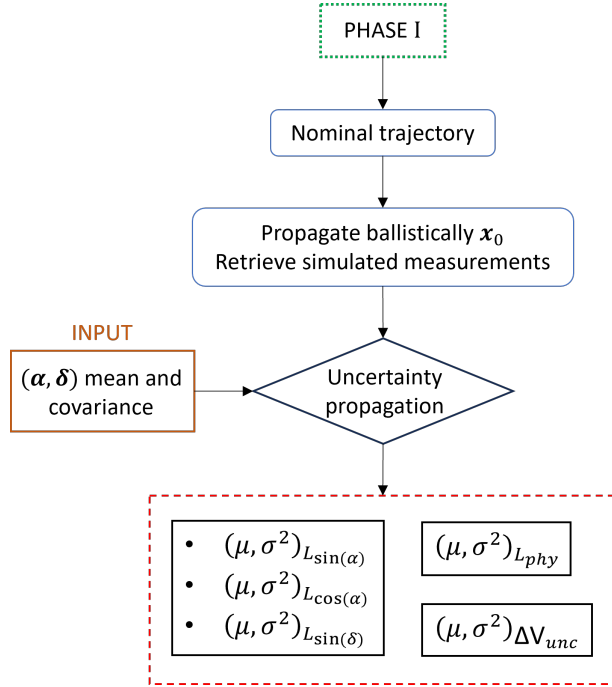
By applying the same procedure explained in Subsec-

Fig. 5. Flowchart Phase II ([14]). In red are highlighted the quantities of interest to define the correlation index.

tion 3.1.1 to each sample, the desired probability distributions (i.e. mean and covariance) of the quantities of interest needed for the correlation index are retrieved:

- $(\mu, \sigma^2)_{L_{phy}}$: probability distribution of physics losses.

- $(\mu, \sigma^2)_{L_{BCs}}$: probability distribution associated to the boundary conditions losses.

- $(\mu, \sigma^2)_{\Delta V_{unc}}$: recalling the hypothesis made at the beginning, no maneuvering objects are considered. Thus, ideally, the ΔV associated to the nominal trajectory is sufficiently small to be attributed to uncertainties, represented by this distribution.

3.1.3 Phase III: Correlation

Finally, the correlation is assessed to statistically determine whether two different tracklets can be associated with the same object. This process involves evaluating the distances between the nominal values and the distributions computed in the earlier phases. By comparing these distances, the method establishes a meaningful correlation between the tracklets, thereby verifying if they pertain to the same object. In the realm of track-to-track association, the commonly used Figure of Merit (FoM) is the Squared Mahalanobis Distance (SMD). This metric quantifies the

distance between a point and a multivariate probability distribution. Hence, the SMD is defined as follows:

$$SMD = (\boldsymbol{V}_{nom} - \boldsymbol{\mu}_{\boldsymbol{V}_{unc}})^T \boldsymbol{P}_{\boldsymbol{V}_{unc}}^{-1} (\boldsymbol{V}_{nom} - \boldsymbol{\mu}_{\boldsymbol{V}_{unc}}) \quad (33)$$

where $\boldsymbol{V}$ is a vector including the 5 contributions, respectively for the nominal and the uncertainty cases:

$$\boldsymbol{V}_{nom} = [L_{phy}, L_{\sin\alpha}, L_{\cos\alpha}, L_{\sin\delta}, \Delta V_{nom}]^T \quad (34)$$

$$\boldsymbol{V}_{unc} = \left[\mu_{L_{phy}}, \mu_{L_{\sin\alpha}}, \mu_{L_{\cos\alpha}}, \mu_{L_{\sin\delta}}, \mu_{\Delta V_{unc}}\right]^T \quad (35)$$

The SMD is assumed to follow a chi-squared χ^2 distribution, which represents the distribution of probability defined by the sum of the squares of n_x random variables with a standard normal distribution. Thus, the SMD is distributed as a χ^2 with n_x degrees of freedom (in this case, $n_x = 5$), and is associated to a significance level s_L, which is set to the 3σ value (i.e., 0.9973) ([29]). This procedure, known as the χ^2-test, enables the classification of two tracklets as either correlated or uncorrelated. According to [30], the correlation index (P_C) can be expressed as:

$$P_C = \frac{SMD}{\chi^2} \quad (36)$$

Within this framework, two tracklets are assumed to belong to the same object if the associated correlation index meets the following criterion:

$$P_C \leq \theta_C \quad (37)$$

where θ_C is the correlation threshold. While it is generally set to 1, it can be modified based on the performance index values or to enhance a specific performance metric.

Indeed, correlation is assessed based on three main performance metrics:

- Recall
  It represents the percentage of identified objects relative to the total number of objects observed:

$$Recall = \frac{TP}{TP + FN} \quad (38)$$

  where TP denotes the true positives, while the missed objects are referred to as false negatives (FN).

- Specificity
  It measures the method's effectiveness in identifying non-correlated observations. Specifically, it is the percentage of correctly identified non-correlated

pairs out of the total number of negative combinations tested.

$$Specificity = \frac{TN}{TN + FP} \qquad (39)$$

where TN represents the true negatives, and the incorrectly correlated objects are referred to as false positives (FP).

- Accuracy
  Here, balanced accuracy is used to address the issues arising from imbalanced datasets. Specifically, the datasets analyzed contain a significantly higher number of negative associations compared to positive ones. To mitigate this issue, the accuracy is defined as follows:

$$Accuracy = \frac{Recall \times Specificity}{2} \qquad (40)$$

where $Recall$ and $Specificity$ are normalized metrics that account for the entire population of positive and negative cases, respectively.

4. Numerical Results

This section presents the outcomes derived from applying the proposed approach to both simulated and real angles-only observational data. The results are critically analyzed, highlighting the method's strengths and weaknesses to identify potential areas for improvement.

The framework's parameters are configured to balance efficiency and performance. The neural network is set with $n = 50$ collocation points, $L = 20$ neurons in the hidden layer, and utilizes a sigmoid activation function. This specific setup has been selected through a trial-and-error process, as it provides a good trade-off between computational time and generalization capabilities, ensuring convergence in most cases. For all applications, the outer layer weights, $\boldsymbol{\beta}$, are randomly initialized within the range of -1 to 1. The loss weights are defined by the following scalar values, equal for all the components of the corresponding vectors:

$$\begin{aligned} W_{phy} &= 10^{-1} \\ W_{BCs} &= 100 \\ W_E &= 100 \end{aligned} \qquad (41)$$

These values, in conjunction with the network structure, enable effective convergence to the best energy-optimal trajectory for each association. Uncertainty propagation is managed using a Monte Carlo simulation with 100 samples, which provides sufficiently accurate results while keeping the computational load contained.

The Pontryagin Neural Network algorithm consistently converges to a solution. However, since the datasets have been automatically generated using the first and last tracklets for each object, some cross-combinations are not feasible due to overlapping observation times. These cases have been removed from the analysis without impacting the study. The results are labeled as follows:

- $\boxed{P_C} \rightarrow$ successful correlation.

- $—\ \rightarrow$ overlapped tracklets.

Here, P_C refers to the correlation index defined in Subsection 3.1.3.

4.1 Validation

A preliminary validation of the approach is conducted using a dataset simulated with the aim of faithfully reproducing some real measurements, collected in a dataset named $\mathcal{D}_3$. In this approach, only the first and last tracklets for each object are considered. The simulation process begins by retrieving the object's state at the TLE epoch. This state is then propagated to each measurement epoch, allowing the generation of a set of observations. These observations are then adjusted to account for the instrument's uncertainty $\sigma = 10^{-6} rad$ (Eq. 32). Thus, the generated dataset is composed by non-equidistant simulated observations of 9 GEO satellites with time intervals between tracklets in the range $1 - 8$ hours, mostly around 7 hours.

It is important to note that the measurements have been simulated using an unperturbed two-body dynamical model, which is the same model employed in the method's algorithm. Therefore, the correlation results are expected to be more favorable than in real applications.

Furthermore, two sensitivity analyses are carried out on reduced datasets of five objects characterized by equidistant measurements. Specifically, the influence of two parameters defining the acquisition process of an optical survey is evaluated:

- Δt_{obs}: acquisition period.
  Fixing $ToF = 7\ h$, while varying the Δt_{obs} across the following values:
  $$\Delta \boldsymbol{t}_{obs} = [20, 100, 500, 1000]\ s \qquad (42)$$

- ToF: time distance between tracklets belonging to the same object.
  Fixing $\Delta t_{obs} = 100s$, while varying the ToF across the following values:
  $$\boldsymbol{ToF}_{vect} = [3, 7, 24]\ h \qquad (43)$$

To complete the correlation criterion, the correlation threshold must be specified (Subsection 3.1.3). While θ_C can be set arbitrarily in some cases, this validation phase uses a threshold of 1 to maintain a 3σ confidence level. Therefore, the performance index P_C must satisfy the following condition:

$$\chi^2(n_x, s_L) = 18.205 \quad \rightarrow \quad P_C = \frac{SMD}{\chi^2} \leq 1 \quad (44)$$

4.1.1 Simulated Dataset

The correlation results obtained by applying the PoNN-based method to the simulated data are reported below. For demonstration purposes, Table 2 shows the values taken by the correlation index P_C for the first 5 objects. Each row represents the first tracklet (i.e. the first observed object), while each column denotes the object associated to the second series of measurements. Correlated and uncorrelated tracklets couples are displayed in Fig. 6.

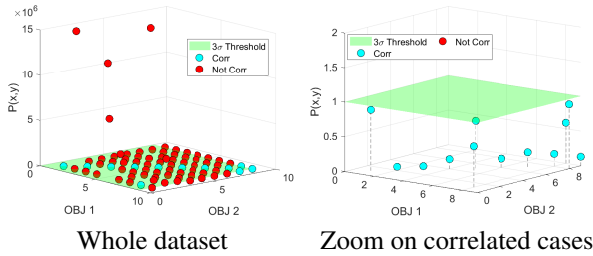|	#1	#2	#3	#4	#5
#1	0.877	10^7	929	85.83	1942
#2	11.95	0.0491	519	285	428
#3	395	—	0.0490	$2{\cdot}10^5$	10^4
#4	105	$6{\cdot}10^6$	2143	0.14	277
#5	10^7	$2{\cdot}10^6$	4575	14.14	0.682

Table 2. P_C simulated dataset.

Fig. 6. Correlated (blue) and uncorrelated (red) associations.

Correlation performance is summarized in terms of recall, specificity and accuracy (Fig. 7). The results highlight the method's ability to correctly identify all observed objects, achieving a recall of 100%. Moreover, the method exhibits a promising behaviour, as PoNN effectively identifies non-correlated associations, significantly reducing the number of false positives. These considerations are

quantitatively reflected in Table 3. Additionally, it is important to consider the dataset's imbalance when interpreting these results, as there is a significant excess of negative associations compared to the potential number of detectable objects.
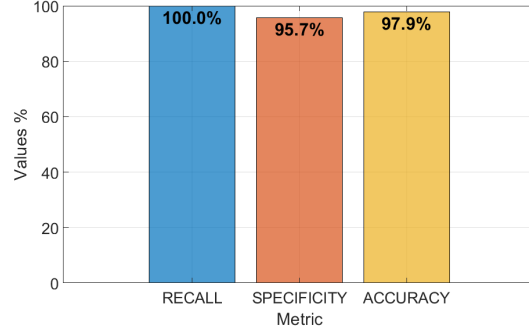

Fig. 7. Performance validation.

P	N	TP	TN	FP	FN
9	70	9	67	3	0

Table 3. Results validation.
(P=Positives, N=Negatives, TP=True Positives, TN=True Negatives, FP=False Positives, FN=False Negatives)

4.1.2 Sensitivity Analysis on Δt_{obs}

This analysis seeks to evaluate the impact of the acquisition time parameter Δt_{obs}, defined as the time between two successive observations of the same tracklet, on the method's performance. To achieve this, multiple tests are conducted using different Δt_{obs}, while keeping ToF constant.

$\Delta t_{obs}(s)$	Recall (%)	Specificity (%)	Accuracy (%)
20	60	68.4	64.2
100	100	100	100
500	100	100	100
1000	100	100	100

Table 4. Correlation for varying Δt_{obs} ($ToF = 7$ hours).

Table 4 indicates that performance improves with longer observation acquisition intervals. The algorithm appears to converge more quickly and efficiently to the energy-optimal solution when measurements are spaced farther apart, as indicated by the computational time trend shown below (Fig. 8). However, also excessive spacing

between observations can result in diminished computational efficiency.

This behavior resembles that of classical orbit determination techniques, such as those developed by Gauss and Laplace, which necessitate measurements spaced at adequate intervals in order for the method to be geometrically well-posed and for the pure Keplerian dynamics assumption to hold. As a result, the motion of GEO satellites is represented with higher accuracy in this last case scenario.
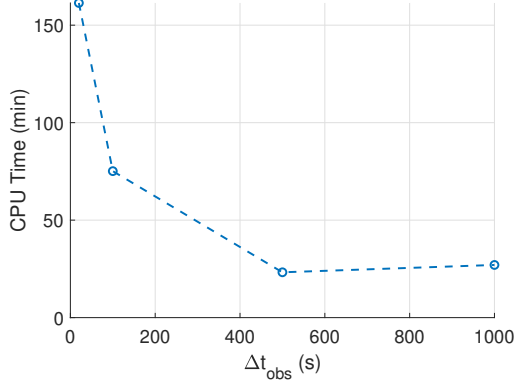

Fig. 8. Computational time for varying Δt_{obs}.

4.1.3 Sensitivity Analysis on ToF

By applying the same reasoning, the impact of the time of flight on the results is evaluated by setting Δt_{obs} to 100 seconds and varying the time of flight to 3, 7, or 24 hours (Table 5). It should be noted that the 24-hour case represents a worst-case scenario.

$ToF(h)$	Recall (%)	Specificity (%)	Accuracy (%)
3	100	100	100
7	100	100	100
24	0	100	50

Table 5. Correlation for varying ToF ($\Delta t_{obs} = 100$ s).

As the distance between tracklets increases, the method's ability to identify correlated associations decreases. Specifically, when ToF exceeds the duration of a single night, no correlated tracklets are detected, causing the recall to drop to zero and the specificity to reach 100%. This indicates that the method, in its current formulation and implementation, is effective for tracklets collected within the same night but becomes unsuitable for measurements separated by longer time spans.

As expected, the computational time required to analyze all potential associations increases with the tracklets distance. While it remains manageable for data from the

same night, it grows significantly when associating measurements from different nights (Fig. 9).
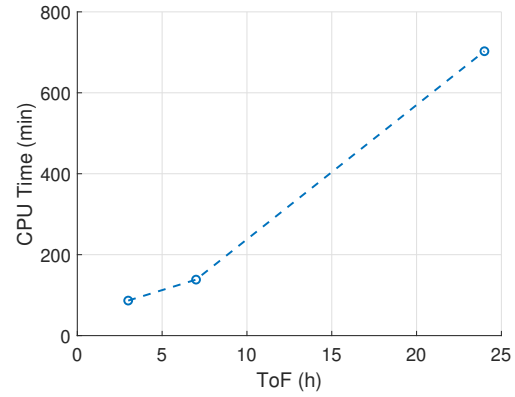

Fig. 9. Computational time for varying ToF.

4.2 Real Data

The available real angles-only observations have been divided according to the acquisition strategy.

Datasets $\mathcal{D}_{1,2}$ These observations consist of series of tracklets from 4 GEO satellites, with each tracklet comprising 3 observations spaced 20 seconds apart. They have been organized into two datasets, denoted as $\mathcal{D}_{1,2}$, based on the specific tracklets included. $\mathcal{D}_1$ is composed by the first and last tracklets of the night for each object, with significant time intervals among the tracklets around $8 - 12$ hours. On the contrary, $\mathcal{D}_2$ includes the first and second tracklets for the first 3 objects, while the first tracklet of the $4th$ object is paired with its third tracklet to ensure adequate separation. Consequently, this dataset is characterized by shorter times of flight (3 to 6 h).

Datasets $\mathcal{D}_{3,4,5,T}$ These real topocentric right ascension and declination measurements of 34 GEO satellites have been provided by the telescopes of the Space4 Center at the University of Arizona. From these observations, 4 datasets have been built by considering the first and last tracklets for each observed object, leading to times of flight between 1 and 8 hours. However, without further information on the acquisition strategy, it can only be reported that the observation intervals, Δt_{obs}, vary between 70 and 800 seconds. Each dataset contains information about nine objects, except for $\mathcal{D}_5$, which is composed by observations of 7 satellites.

4.2.1 Correlation Threshold

Unlike in the validation phase, the correlation index P_C exhibits a generally higher trend. Therefore, by applying the method to a dataset $\mathcal{D}_T$, a suitable threshold can be

determined through a trial-and-error process. To achieve balanced overall performance, the correlation threshold θ_C has been set at 150. Table 6 displays the normalized values of P_C for 5 satellites.

	#1	#2	#3	#4	#5
#1	1.638	83.28	345	493	371
#2	—	2.335	349	369	421
#3	6218	245	0.184	17.70	0.303
#4	1172	3542	0.123	0.7	0.0371
#5	726	226	3934	0.6	0.0053

Table 6. P_C normalized for dataset $\mathcal{D}_T$.

Therefore, the tracklets association's criterion can be reformulated as follows:

$$\chi^2(n_x, s_L) = 18.205 \quad \rightarrow \quad P_C = \frac{SMD}{\chi^2 \cdot \theta_C} \leq 1 \quad (45)$$

4.2.2 Test

This section presents the tests conducted on the remaining five datasets. The PoNN-based framework is configured as during validation (Section 4), with one exception: the number of neurons needed to solve $\mathcal{D}_1$. Due to the longer flight times in this dataset, ranging from 8 to 12 hours, the number of neurons in the hidden layer have been increased to 30. This adjustment ensured successful convergence, producing outcomes consistent with those observed in the other cases.

The results are displayed in Fig. 10 and summarized below in Table 7.

	$\mathcal{D}1$	$\mathcal{D}2$	$\mathcal{D}3$	$\mathcal{D}4$	$\mathcal{D}5$
R (%)	100	75	88.9	66.7	71.4
S (%)	66.7	91.7	82.9	71.8	85.4
A (%)	83.3	83.3	85.9	69.2	78.4
t (min)	554.78	51.62	65.17	104.5	67.9

Table 7. Summary results.
(R=Recall, S=Specificity, A=Accuracy, t=CPU Time)

Given that the simulated data used for validation have been designed to replicate the dataset $\mathcal{D}_3$, a direct comparison can be made. This reveals a decrease in performance when applying the method to collections of real data. In the simulated case, the algorithm easily solves the problem since the measurements have been generated using a simple two-body dynamical model, which aligns with the dynamics on which the algorithm is based. However, in a real-world scenario, the observations are produced by satellites following perturbed two-body dynamics, where several factors influence the motion, such as the gravitational perturbations related to J2 and J22, the third body perturbation of the Sun and the Moon, and the solar radiation pressure. Consequently, this introduces a significant discrepancy between the dynamical models employed by the algorithm and the actual conditions governing the real observations. As expected, real measurements are more challenging to correlate. However, the results highlight that, despite the increased difficulty in object detection, the number of false positives remains low. Therefore, the detected satellites are associated with a higher confidence level, indicating that successful correlations are likely to represent actual physical objects.

Additionally, it is observed that the correlation performance for $\mathcal{D}_1$ slightly differs from the other datasets. This variation can be attributed to the longer time intervals between the tracklets characterizing this dataset. As associations involving more distant tracklets are tested, the likelihood of detecting objects increases, yet at the expense of a higher number of false positives.

The primary drawback of this method is its significant computational burden limiting the method's applicability when analyzing a large number of associations. Dataset $\mathcal{D}_1$ particularly suffers from prolonged solution times due to the higher number of neurons used. However, interestingly, the dataset $\mathcal{D}_3$, which consists of 9 satellites, is solved in less time than $\mathcal{D}_1$, which contains only 4 objects. This may suggest that computational time is more influenced by the type of measurements and the observed objects than by the size of the dataset itself.

5. Conclusions

The importance of this work is highlighted by its potential to enhance space situational awareness (SSA) and improve the safety of space operations. SSA is a crucial field that involves understanding the space environment, including the positions and trajectories of both natural and artificial objects orbiting Earth. By properly correlating optical observations, the proposed method contributes to more effective monitoring of the orbital environment. This capability is becoming crucial as the space industry expands into the X-GEO region, where new techniques for correlating and identifying space objects under diverse dynamical conditions will be essential.

In this context, the proposed PoNN-based method is shown to be promising. It operates effectively even with-
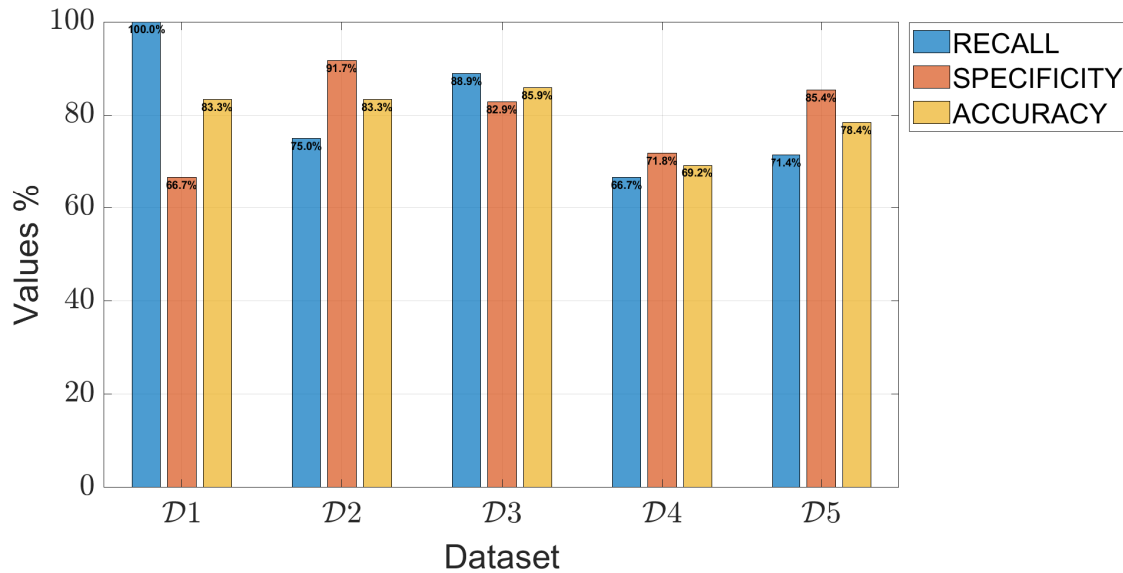
Fig. 10. Results real datasets.

out providing any initial orbit estimates or admissible regions, proving robustness even when satellite orbit information is unavailable. This is achieved by directly approximating the state and costate variables using constrained expressions within the PoNN framework. Indeed, the developed approach is already prone to be applied to other dynamical regimes, and will definitely be part of future works. The obtained results are quite consistent across the several analyzed datasets, with a tendency to minimize the number of false positive cases, thus leading to a more reliable objects detection. Nevertheless, there is room for improvement mainly to reduce the computational time required by this method. Enhancements could include refining PoNN's uncertainty propagation or utilizing a more efficient computational environment.

Acknowledgements

References

[1] EUSPA. (Apr. 29, 2024), [Online]. Available: https://www.euspa.europa.eu/eu-space-programme/ssa.

[2] CelesTrak. "Recent debris event." (2007), [Online]. Available: https://celestrak.org/events/debris-events.php.

[3] P. Laplace, "Mém. acad. r. sci. paris," in *Laplace's collected works*, 1780.

[4] C. F. Gauss, "Theoria motus corporum coelestium in sectionibus conicis solem ambientium: Frontmatter," 2011.

[5] D. A. Vallado, "Fundamentals of astrodynamics and applications," 1997.

[6] G. Tommei, A. Milani, and A. Rossi, "Orbit determination of space debris: Admissible regions," *Celestial Mechanics and Dynamical Astronomy*, vol. 97, Apr. 2007. DOI: 10.1007/s10569-007-9065-x.

[7] A. Milani, G. F. Gronchi, M. De' Michieli Vitturi, and Z. Knezevic, "Orbit determination with very short arcs. i - admissible regions," *Celestial Mechanics and Dynamical Astronomy*, vol. 90, pp. 57–85, Jul. 2004. DOI: 10.1007/s10569-004-6593-5.

[8] K. DeMars and M. Jah, "Probabilistic initial orbit determination using gaussian mixture models," *Journal of Guidance Control Dynamics*, vol. 36, pp. 1324–1335, Sep. 2013. DOI: 10.2514/1.59844.

[9] D. Farnocchia, G. Tommei, A. Milani, and A. Rossi, "Innovative methods of correlation and orbit determination for space debris," Nov. 2009.

[10] G. Tommei, A. Milani, D. Farnocchia, and A. Rossi, "Correlation of space debris observations by the virtual debris algorithm," in *Proc. '5th European Conference on Space Debris'*, ESA SP-672, 2009.

[11] G. F. Gronchi, L. Dimare, and A. Milani, "Orbit determination with the two-body integrals," *Celestial Mechanics and Dynamical Astronomy*, vol. 107, Nov. 2009. DOI: 10.1007/s10569-010-9271-9.

[12] G. F. Gronchi, D. Farnocchia, and L. Dimare, "Orbit determination with the two-body integrals. ii," *Celestial Mechanics and Dynamical Astronomy*, vol. 110, pp. 257–270, Jul. 2011. DOI: 10.1007/s10569-011-9357-z.

[13] A. De Riz, R. Cipollone, and P. Di Lizia, "An automatic domain splitting initial orbit determination technique for short-arc optical measurements," M.S. thesis, Politecnico di Milano, 2022.

[14] L. Ramponi, R. Cipollone, A. De Riz, A. D'Ambrosio, R. Furfaro, and P. Di Lizia, "Optical track-to-track correlation with differential algebra and pontryagin neural networks," M.S. thesis, Politecnico di Milano, 2024.

[15] M. J. Holzinger, D. J. Scheeres, and K. T. Alfriend, "Object correlation, maneuver detection, and characterization using control distance metrics," *Journal of Guidance, Control, and Dynamics*, vol. 35, no. 4, pp. 1312–1325, 2012. DOI: 10.2514/1.53245.

[16] A. D'ambrosio, E. Schiassi, F. Curti, and R. Furfaro, "Pontryagin neural networks with functional interpolation for optimal intercept problems," *Mathematics*, vol. 9, no. 9, p. 996, 2021.

[17] M. Raissi, P. Perdikaris, and G. Karniadakis, "Physics-informed neural networks: A deep learning framework for solving forward and inverse problems involving nonlinear partial differential equations," *Journal of Computational Physics*, vol. 378, Nov. 2018. DOI: 10.1016/j.jcp.2018.10.045.

[18] G. V. Cybenko, "Approximation by superpositions of a sigmoidal function," *Mathematics of Control, Signals and Systems*, vol. 2, pp. 303–314, 1989.

[19] K. Hornik, M. Stinchcombe, and H. White, "Multilayer feedforward networks are universal approximators," *Neural Networks*, vol. 2, no. 5, pp. 359–366, 1989, ISSN: 0893-6080. DOI: https://doi.org/10.1016/0893-6080(89)90020-8.

[20] E. Schiassi, R. Furfaro, C. Leake, M. De Florio, H. Johnston, and D. Mortari, "Extreme theory of functional connections: A fast physics-informed neural network method for solving ordinary and partial differential equations," *Neurocomputing*, vol. 457, pp. 334–356, 2021, ISSN: 0925-2312. DOI: https://doi.org/10.1016/j.neucom.2021.06.015.

[21] A. Scorsoglio, A. D'Ambrosio, L. Ghilardi, R. Furfaro, and V. Reddy, "Physics-informed orbit determination for cislunar space applications," in *In Proceedings of the Advanced Maui Optical and Space Surveillance (AMOS) Technologies Conference, Wailea, HI (p. 10).*, 2023.

[22] A. Scorsoglio, A. D'Ambrosio, T. Campbell, R. Furfaro, and V. Reddy, "Orbit determination pipeline for geostationary objects using physics-informed neural networks," in *AIAA SCITECH 2024 Forum*, 2024, p. 1862.

[23] A. D'Ambrosio, "Optimal guidance and control for space missions on asteroids and planetary bodies," Ph.D. dissertation, Sapienza Università di Roma, Dec. 2021.

[24] D. Mortari, "The theory of connections: Connecting points," *Mathematics*, vol. 5, no. 4, 2017, ISSN: 2227-7390. DOI: 10.3390/math5040057.

[25] H. R. Johnston, "The theory of functional connections: A journey from theory to application," Ph.D. dissertation, Texas A&M University, 2021.

[26] G.-B. Huang, L. Chen, and C. Siew, "Universal approximation using incremental constructive feedforward networks with random hidden nodes," *IEEE transactions on neural networks / a publication of the IEEE Neural Networks Council*, vol. 17, pp. 879–92, Jul. 2006. DOI: 10.1109/TNN.2006.875977.

[27] G.-B. Huang, Q.-Y. Zhu, and C.-K. Siew, "Extreme learning machine: Theory and applications," *Neurocomputing*, vol. 70, no. 1, pp. 489–501, 2006, Neural Networks, ISSN: 0925-2312. DOI: https://doi.org/10.1016/j.neucom.2005.12.126.

[28] E. D. Gustafson and D. J. Scheeres, "Optimal timing of control-law updates for unstable systems with continuous control," *Journal of Guidance, Control, and Dynamics*, vol. 32, no. 3, pp. 878–887, 2009. DOI: 10.2514/1.38570.

[29] L. Pirovano, R. Armellin, J. Siminski, and T. Flohrer, "Differential algebra enabled multi-target tracking for too-short arcs," *Acta Astronautica*, vol. 182, Feb. 2021. DOI: 10.1016/j.actaastro.2021.02.023.

[30] M. F. Montaruli *et al.*, "An orbit determination software suite for space surveillance and tracking applications," *CEAS Space Journal*, vol. 16, Mar. 2024. DOI: 10.1007/s12567-024-00535-1.